Agile Maneuvers for Push-Broom Imaging Satellites

Dennis D. Langer, *Member, IEEE,* Joseph L. Garrett, *Member, IEEE,* Bjørn A. Kristiansen, *Member, IEEE,* Sivert Bakken, *Member, IEEE,* Simen Berg *Graduate Student Member, IEEE,*, Roger Birkeland, *Member, IEEE,* J. Tommy Gravdahl, *Senior Member, IEEE,* Tor A. Johansen, *Senior Member, IEEE,* Asgeir J. Sørensen, *Senior Member, IEEE*

***Abstract*—Traditional large Earth Observation Satellites (EOS) are designed with simple imaging strategies. However, small satellites can satisfy immediate user needs through agile imaging modes. In this paper, we model several agile imaging mode concepts and test them experimentally on the push-broom hyperspectral imaging cubesat HYPSO-1. Six imaging modes are tested: slewing, multi-target, dual-angle, wide swath, on-board processing, and dynamic pointing. The results show that the slewing and multi-angle mode increased estimated Signal-to-Noise Ratio (SNR) by 1.4x to 1.7x, the on-board processing mode decreased data latency, and the multi-target, wide swath and dynamic pointing modes enhanced spatial coverage.**

***Index Terms*—Remote sensing, satellite scheduling, attitude control, agile operations, Hyperspectral, imaging spectroscopy.**

I. Introduction

ALL satellites operate within constraints defined by orbital mechanics. For an Earth Observation Satellite (EOS), the orbit influences coverage as well as spatial and temporal resolution, e.g., the revisit time of a given area. For example, a geostationary satellite may possess high temporal resolution, as it can observe the same location continuously but cannot cover all possible target locations on Earth. On the other hand, a satellite in Low Earth Orbit (LEO) can achieve better spatial resolution and can potentially cover all target locations on Earth if placed in an orbit with high enough inclination. However, this leads to a longer revisit time, as the satellite does not pass over the same location in consecutive orbits. By varying orbital altitude, spatial resolution may be exchanged for temporal resolution, or vice-versa.

Attitude control can be used to increase the temporal resolution of EOSs in LEO. For example, while traditional EOSs like Sentinel-3 point at a constant angle relative to nadir [1], others can decrease their revisit time by pointing off-nadir in one degree of freedom [1]–[4]. Without pointing, an EOS has to wait until a target of interest falls into the swath of a statically pointing instrument, typically right below the satellite's orbital track. Temporal resolution is increased by pointing towards a target even though it may not be right below the satellite's orbital track. This pointing process is also called satellite tasking.

Further capabilities are achievable by agile EOS, which have the ability to point their instrument(s) in two or more degrees of freedom [5], for example simultaneously pointing ahead in the along track direction and pointing off-nadir across track. This is especially useful when considering multiple targets simultaneously, where imaging a target by pointing with a single degree of freedom may remove the opportunity to image another target that is located close-by. In this article, the term 'agile' is understood in two ways. Agile pointing as just described and 'agile operations', in which operational functionality is extended beyond the pre-launch mission Concept of Operations (CONOPS) by use of new procedures and software updates. The latter meaning is discussed later in this section.

Agile EOSs can complement traditional satellites by using specialized sensors with narrower field of view that prioritize particular locations over global coverage. With agile pointing, the specialized sensors can observe the prioritized targets of interest in larger detail than traditional EOS.

Agile EOSs maneuvers can be put into two groups: Conventional Agile Earth Observation Satellites (CA-EOSs) and Super Agile Earth Observation Satellites (SA-EOSs) [6]. A CA-EOS maneuver consists of a attitude changes in-between image acquisitions while keeping a nearly fixed orientation during image acquisition. This constrains the scanning direction in the along track direction. For example, the PROBA-1 satellite generally records five sequential images of a target, each at different angles while compensate for its velocity [7]. Such multi-angle observations have also contributed to the accuracy of aerosol depth measurements [8]. Likewise, rotations in the yaw direction enabled the side-slither relative radiometric calibration technique, used on both the QuickBird multispectral satellite and the Ziyuan-1(02D) hyperspectral satellite [9], [10].

In contrast, SA-EOSs maneuvers are defined by active pointing during an image acquisition. This enables arbitrary, non-along-track scanning directions as well as scanning along curved target tracks. SA-EOSs require active pointing control at high rotational speeds during the whole imaging period, and thus increases the demands on the Attitude Determination and Control System (ADCS) subsystem. Super-agility has enabled a number of qualitatively distinct imaging modes.

Manuscript received 16 October 2023. This work was supported by the Research Council of Norway through the Centre of Excellence funding scheme NTNU AMOS (grant no. 223254), HYPSCI (grant no. 325961), Green-Platform (grant no. 328724), and EEA NO Grants 2014 - 2021 under Project ELO-Hyp (contract no. 24/2020). (*Corresponding author: Dennis D. Langer*)

Dennis D. Langer and Asgeir J. Sørensen are with the Department of Marine Technology, Norwegian University of Science and Technology (NTNU), 7034 Trondheim, Norway (e-mail: dennis.d.langer@ntnu.no; asgeir.sorensen@ntnu.no). Joseph L. Garrett, Bjørn A. Kristiansen, Simen Berg, J. Tommy Gravdahl and Tor A. Johansen are with the Department of Engineering Cybernetics, Norwegian University of Science and Technology (NTNU), 7034 Trondheim, Norway. Sivert Bakken is with SINTEF Ocean AS, Trondheim, Norway. Roger Birkeland is with the Department of Electronic Systems, Norwegian University of Science and Technology (NTNU), 7491 Trondheim, Norway.

For example, pitch motion compensation can decrease Ground Sample Distance (GSD) and increase the Signal-to-Noise Ratio (SNR) [11], [12] or widening the coverage around a target by dynamic pointing towards a target point below the Earth's surface [13]. Similarly, it can track sun-glint to enable gas detection over water surfaces [14]. Furthermore, laboratory experiments suggest that SA-EOSs could scan along geographic boundaries [15]. The Agile MicroSat is a technology demonstrator that features agile pointing and orbit control to increase the ability to revisit a target location more often [16], [17].

The commercial high spatial resolution EOS from Maxar [18] (e.g. GeoEye [19], WorldView [20]), Planet (SkySat [21], and the planned Pelican constellation [22]) and Pléiades [23] feature agile tasking for imrpoved target revisit time. The Pleiades Imagery User Guide [24] describes several agile modes, both CA-EOS and SA-EOS, like multi-angle imaging, and linear non-along track scanning. The Space View Technology's SuperView satellite series features similar agile pointing capabilities as WorldView, with multi-angle and multi target imaging, and slewing [25].

While pointing agility greatly expands the capabilities of EOSs, it also expands the complexity of image acquisition scheduling. The agile imaging scheduling problem was formalized in 2002 in connection with the Pléiades constellation [5]. The article introduces several simplifications, including a limitation on super-agile maneuvers. The problem has been extended to incorporate multiple objectives, online scheduling, and satellite constellations [26]–[29]. In [30], the authors give a review of the literature related to the agile EOS imaging scheduling problem. The scheduling problem becomes more computationally intensive when super-agile maneuvers are permitted. To reduce the number of possible solutions, attempts to solve the super-agile scheduling problem divide the solution into two steps, the first defines a set of atomic tasks for imaging target locations, and the second selects between these atomic tasks [6], [31].

Push-broom instruments complicate agile pointing by requiring a specific scanning direction. Snapshot instruments could leave the orientation around the view direction unspecified, while still observing a target. In contrast, a push-broom instrument requires that its slit aperture is oriented to the desired scan path in some way, e.g. perpendicularly, for target observation. This means the attitude for a satellite with a snapshot instrument can leave one degree of freedom unspecified, while the attitude needs to be specified fully for a satellite with push-broom instrument. This also complicates the agile imaging scheduling problem.

Agility may also be expressed in terms of operational agility utilizing on-board processing capabilities. On-board processing can be a solution for overcoming coverage and downlink bottlenecks, especially for satellites with hyperspectral instruments that feature large data sizes. For example, the Copernicus Hyperspectral Imaging Mission for the Environment (CHIME) is planned to feature adaptive data compression based on identified cloud content [32]. The Intuition-1 mission launched a 6U cubesat for testing machine learning algorithms for hyperspectral data processing [33]. The Φ-Sat-1 satellite demonstrated on-board cloud segmentation on images captured using the HyperScout-2 instrument [34]. The OPS-SAT satellite is a platform for testing new satellite control software, including image processing and machine learning models trained on-board the satellite after launch [35], [36]. However, the OPS-SAT has no imaging payload and a more general scope than earth observation. The LuoJia3-01 satellite has demonstrated utilization of on-board processing for low-latency RGB video delivery directly to an end user. The HYPerspectral Smallsat for Ocean observation satellite 1 (HYPSO-1) mission demonstrated on-board Support Vector Machine (SVM) classification of hyperspectral images [37]. As opposed to CHIME, the OPS-SAT, Φ-Sat-1 and Intuition-1 feature on-board processing in an agile sense, adding new functionality using on-board software updates.

Although the number of agile EOS is large, featuring both snapshot and push-broom instrument design, the scientific literature lacks documentation of the attitude planning method used for these missions. Satellite missions usually operate according to a CONOPS that is fixed before launch and do not investigate the full range of possibilities that agile operations could provide.

Our contribution is a simple and modular attitude planning method that can be used for numerous kinds of agile maneuvers that an EOS with a push broom instrument can perform. We test it through several experimental demonstrations. We use HYPSO-1 [38], [39] as a case study. We compare various agile and super-agile atomic tasks to a baseline, non-agile maneuver. The tasks increase SNR and enhance coverage. The operational flexibility that an in-house developed Commercial Off-The-Shelf (COTS) small satellite payload provides is utilized to perform several operations that were not described in the original pre-launch description of the CONOPS [38]. We also demonstrate a low-latency tasking and data downlink procedure similar to [40], except that we are using hyperspectral data segmentation algorithms.

The paper is organized as follows: Section II provides relevant background context and definitions. Section III expands on the agile EOS capture modes. Section V shows the results and discussions from performing the capture modes with HYPSO-1. Finally, Section VI contains conclusions of the work.

II. Background

In the following sections, we present background knowledge and terminology used in this paper.

A. Push-broom imaging

Push-broom imaging is characterized by a scanning procedure to form an image. A push-broom imager, also known as a line scan camera, usually consists of a linear pixel array that generates an image by collecting several linear snapshots, or lines, while sweeping across an area [41], [42]. Figure 1 illustrates the geometry of a push-broom imager. For CA-EOS, the direction in which the imager sweeps is parallel to the satellite's ground track. This direction is called along track, and the direction perpendicular to along track is called

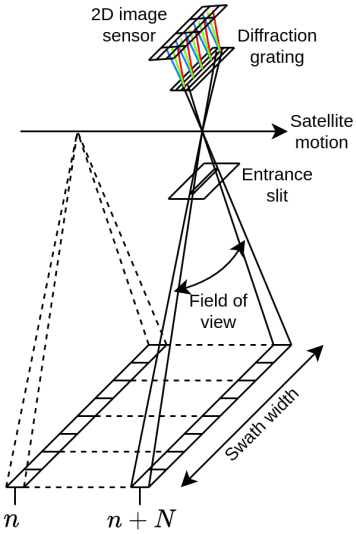

Fig. 1: Illustration of a diffraction grating hyperspectral push-broom imaging geometry. An area is observed after scanning a number of lines.

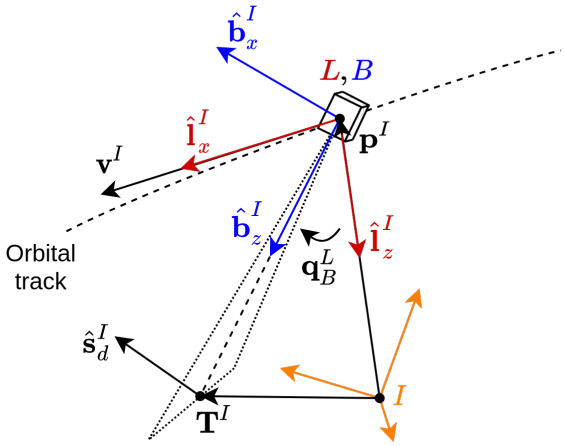

Fig. 2: Illustrating the relevant reference frames and some of their coordinate axes, as well as quantities from which the pointing quaternion $\mathbf{q}_B^L$ is computed: Body frame B, LVLH frame L and the geocentric intertial frame I, e.g. ICRS. The dotted lines indicate the FoV of the push-broom sensor. Target position referenced in ICRS frame is $\mathbf{T}^I$, desired scanning direction referenced in ICRS frame is $\hat{\mathbf{s}}_d^I$ which defines the sensor's yaw rotation. The satellite position vectors is $\mathbf{p}^I$ and velocity vectors is $\mathbf{v}^I$, both referenced in ICRS frame.

across track. The rate of the snapshot collection of frames is determined by the frame rate.

Diffraction-based push-broom hyperspectral imagers usually form a linear pixel array by using an aperture that is long and narrow, passing the slit-shaped light through a diffraction element like a diffraction grating or a prism, and digitizing the light both spectrally and spatially using a 2D pixel array. Scanning allows the creation of a 2D spatial image that contains several bands of light per pixel, also called an hyperspectral image, or data, cube. The opening angle of the push-broom imager along the direction of the linear pixel array is called the Field-of-View (FoV) of the imager. Swath width refers to the length of the FoV when projected onto the Earth. The distance that the ground projected FoV moves from one frame to the next is called the Ground Sample Distance (GSD). The GSD is affected by the frame rate setting of the imager during scanning. Increasing the frame rate decreases the GSD and vice-versa. The GSD can also be influenced by camera motion.

B. Reference frames

See Figure 2 for an illustration of the three relevant coordinate systems. They are the body-fixed reference frame, denoted with a capital 'B', the Local-Vertical Local-Horizontal (LVLH) reference frame, denoted with a capital 'L', and a geocentric International Celestial Reference System (ICRS) frame, denoted with a capital 'I'.

In this paper, the reference frame to which the components of vector quantities that are not representing rotations are referenced in, is denoted with a superscript capital letter corresponding to one of the three reference frames. A subscript x, y or z is added to denote that the vector is a reference frame coordinate axis vector pointing respectively along the x, y or z axis. In addition, a circumflex $\hat{}$ denotes that the vector has unit length. For example, $\hat{\mathbf{b}}_x^I$ is a unit length x-axis vector referenced in the earth centered reference frame.

The body-fixed reference frame, referred to as just the body frame, is an orthonormal coordinate system rigidly attached to the satellite body. Let the body z-axis point along the push broom camera view direction. The body y-axis is defined to point parallel to the entrance slit, i.e., aligned parallel with the captured line at each time instant. The x-axis completes the right-handed coordinate frame, being perpendicular to the push-broom entrance slit. This direction is usually aligned with the push-broom scanning direction. The body frame axis unit vectors referenced in ICRS frame are denoted with $\hat{\mathbf{b}}_x^I$, $\hat{\mathbf{b}}_y^I$ and $\hat{\mathbf{b}}_z^I$.

The LVLH frame is an orthonormal coordinate system that is moving with the EOS's center of mass in its orbit. Its x-axis is aligned with the orbital velocity vector, and the z-axis points from the satellite center of mass to the origin of an Earth-centered reference frame, I. We assume the satellite orbit to be circular. The y-axis completes the right-handed coordinate system. The LVLH frame axis unit vectors referenced in ICRS frame are denoted with $\hat{\mathbf{l}}_x^I$, $\hat{\mathbf{l}}_y^I$ and $\hat{\mathbf{l}}_z^I$.

All imaging maneuvers depend on pointing the satellite to target locations. We consider EOSs that are pointed by specifying a desired attitude to the on-board ADCS. We assume that the attitude is specified by a quaternion $\mathbf{q}_B^L$ that represents the rotation of the satellite body-fixed frame B with respect to the LVLH frame L.

The term nadir refers to the LVLH frame z-axis direction and the the term off-nadir angle is the angle between the LVLH frame z-axis and the body frame imager direction, i.e., the body z-axis.

C. Euler angles and quaternions

We use terminology that is conventionally used in the context of Euler angles, specifically, the terms roll, pitch, and yaw. In this paper, with roll, pitch and yaw, we mean respectively a rotation around the x-axis, y-axis, and z-axis. The coordinate frame to which the axes belong is inferred from the context.

A unit quaternion representing a rotation given by an angle θ and an unit axis vector $\hat{\mathbf{n}} \in \mathbb{R}^3$, $\hat{\mathbf{n}} = [n_x, n_y, n_z]^\top$ is given by

$$\mathbf{q} = \begin{bmatrix} \eta \\ \boldsymbol{\epsilon} \end{bmatrix} = \begin{bmatrix} \cos\frac{\theta}{2} \\ \hat{\mathbf{n}} \sin\frac{\theta}{2} \end{bmatrix} = \begin{bmatrix} \cos\frac{\theta}{2} \\ n_x \sin\frac{\theta}{2} \\ n_y \sin\frac{\theta}{2} \\ n_z \sin\frac{\theta}{2} \end{bmatrix}. \tag{1}$$

A rotation matrix $\mathbf{R} \in \mathrm{SO}(3)$ representing the same rotation can be computed from a unit quaternion, and vice versa. In the following sections, we refer to a unit quaternion representing a rotation as simply a quaternion.

The axis-angle representation of a rotation can be computed from a rotation matrix as follows, assuming $\mathbf{R}$ is not symmetric (Section 6.7.7 in [43])

$$\theta = \cos^{-1}\left(\frac{\mathrm{Trace}\,(\mathbf{R}) - 1}{2}\right) \tag{2}$$

$$\hat{\mathbf{n}} = \frac{1}{2\sin(\theta)} \begin{bmatrix} R_{23} - R_{32} \\ R_{31} - R_{13} \\ R_{12} - R_{21} \end{bmatrix}, \tag{3}$$

where $R_{ij}, i, j \in \{1, 2, 3\}$ are the components of the rotation matrix

$$\mathbf{R} = \begin{bmatrix} R_{11} & R_{12} & R_{13} \\ R_{21} & R_{22} & R_{23} \\ R_{31} & R_{32} & R_{33} \end{bmatrix}. \tag{4}$$

When $\mathbf{R}$ is symmetric, then it describes either no rotation or a rotation of 180 degrees around a single axis. Both cases will rarely occur for satellite tasking when describing a rotation with respect to the LVLH frame. Given our assumptions, a symmetric $\mathbf{R}$ would mean that the satellite is pointing either away from Earth, or pointing exactly nadir.

A series of successive rotations can be combined using the quaternion product. The quaternion product between two quaternions $\mathbf{q}_1 = [\eta_1, \boldsymbol{\epsilon}_1]^\top = [\eta_1, \epsilon_{x,1}, \epsilon_{y,1}, \epsilon_{z,1}]^\top$ and $\mathbf{q}_2 = [\eta_2, \boldsymbol{\epsilon}_2]^\top = [\eta_2, \epsilon_{x,2}, \epsilon_{y,2}, \epsilon_{z,2}]^\top$ is (Section 6.7.4 in [43])

$$\mathbf{q}_1 \otimes \mathbf{q}_2 = \begin{bmatrix} \eta_1\eta_2 - \boldsymbol{\epsilon}_1 \cdot \boldsymbol{\epsilon}_2 \\ \eta_1\boldsymbol{\epsilon}_2 + \eta_2\boldsymbol{\epsilon}_1 + \boldsymbol{\epsilon}_1 \times \boldsymbol{\epsilon}_2 \end{bmatrix} \tag{5}$$

$$= \begin{bmatrix} \eta_1\eta_2 - \epsilon_{x,1}\epsilon_{x,2} - \epsilon_{y,1}\epsilon_{y,2} - \epsilon_{z,1}\epsilon_{z,2} \\ \eta_1\epsilon_{x,2} + \epsilon_{x,1}\eta_2 - \epsilon_{y,1}\epsilon_{z,2} + \epsilon_{z,1}\epsilon_{y,2} \\ \eta_1\epsilon_{y,2} + \epsilon_{x,1}\epsilon_{z,2} + \epsilon_{y,1}\eta_2 - \epsilon_{z,1}\epsilon_{x,2} \\ \eta_1\epsilon_{z,2} - \epsilon_{x,1}\epsilon_{y,2} + \epsilon_{y,1}\epsilon_{x,2} + \epsilon_{z,1}\eta_2 \end{bmatrix}, \tag{6}$$

where $\cdot$ denotes the scalar product and $\times$ denotes the cross product.

III. Method

A. Satellite pointing

This subsection describes the method used to determine the desired pointing attitude (quaternion) $\mathbf{q}^L_{B,d}$ for all described imaging modes except the slewing mode, which will be described in Section III-D. The additional subscript $_d$ denotes *desired*, meaning a user definable quantity that is passed to a system or algorithm to achieve some goal, for example, the reference input to a control system. The desired pointing quaternion $\mathbf{q}^L_{B,d}$ is determined as a function of time t, satellite Two-Line Element (TLE), target location $\mathbf{T}^I$, and desired scanning direction $\hat{\mathbf{s}}^I_d$.

The quaternion is computed from the rotation matrix $\mathbf{R}^L_{B,d}$ rotating between the LVLH frame and the desired body frame. To compute the quaternion $\mathbf{q}^L_{B,d}$ representing the same rotation as the rotation matrix $\mathbf{R}^L_{B,d}$, the rotation matrix is first converted to an axis-angle representation using (2) and (3), followed by computation of the quaternion using (1).

The rotation matrix $\mathbf{R}^L_{B,d}$ is determined from direction cosines that are computed using the unit vectors of the LVLH frame and the desired body frame (Section 6.4.1 in [43])

$$\mathbf{R}^L_{B,d} = \begin{bmatrix} \hat{\mathbf{l}}^I_x \cdot \hat{\mathbf{b}}^I_{x,d} & \hat{\mathbf{l}}^I_y \cdot \hat{\mathbf{b}}^I_{x,d} & \hat{\mathbf{l}}^I_z \cdot \hat{\mathbf{b}}^I_{x,d} \\ \hat{\mathbf{l}}^I_x \cdot \hat{\mathbf{b}}^I_{y,d} & \hat{\mathbf{l}}^I_y \cdot \hat{\mathbf{b}}^I_{y,d} & \hat{\mathbf{l}}^I_z \cdot \hat{\mathbf{b}}^I_{y,d} \\ \hat{\mathbf{l}}^I_x \cdot \hat{\mathbf{b}}^I_{z,d} & \hat{\mathbf{l}}^I_y \cdot \hat{\mathbf{b}}^I_{z,d} & \hat{\mathbf{l}}^I_z \cdot \hat{\mathbf{b}}^I_{z,d} \end{bmatrix}. \tag{7}$$

The LVLH frame x- and z-axis unit vectors given in ICRS frame are computed as follows

$$\hat{\mathbf{l}}^I_x = \frac{\mathbf{v}^I}{||\mathbf{v}^I||} \tag{8}$$

$$\hat{\mathbf{l}}^I_z = -\frac{\mathbf{p}^I}{||\mathbf{p}^I||}, \tag{9}$$

where $\mathbf{p}^I$ is the satellite position vector, and $\mathbf{v}^I$ is the satellite velocity vector. The LVLH frame y-axis is computed via cross-product

$$\hat{\mathbf{l}}^I_y = \hat{\mathbf{l}}^I_z \times \hat{\mathbf{l}}^I_x \tag{10}$$

The desired body axes for pointing to the target are computed using the target position coordinates in ICRS frame, $\mathbf{T}^I$, and a desired scanning direction, $\hat{\mathbf{s}}^I_d$, as follows. The desired body z-axis is pointed towards the target:

$$\hat{\mathbf{b}}^I_{z,d} = \frac{\mathbf{T}^I - \mathbf{p}^I}{||\mathbf{T}^I - \mathbf{p}^I||}. \tag{11}$$

The desired scanning direction $\hat{\mathbf{s}}^I_d$ defines the direction of the desired body x-axis, $\hat{\mathbf{b}}^I_{x,d}$, which is the direction perpendicular to the entrance slit of the push-broom imager. For along track scanning, the scanning direction is set using the satellite velocity vector, $\hat{\mathbf{s}}^I_d = \mathbf{v}^I/||\mathbf{v}^I|| = \hat{\mathbf{l}}^I_x$. For non-along track scanning, the desired scanning direction is set by a different heuristic. If $\hat{\mathbf{s}}^I_d$ is orthogonal to the desired body z-axis, then the desired body x-axis is equal to the scanning direction, $\hat{\mathbf{b}}^I_{x,d} = \hat{\mathbf{s}}^I_d$.

However, $\hat{\mathbf{s}}^I_d$ may not be orthogonal to the desired body z-axis. In this case, the body x-axis needs to be derived from $\hat{\mathbf{s}}^I_d$ and $\hat{\mathbf{b}}^I_{z,d}$ to form the orthonormal axis vectors of the body frame.

One way in which to determine the desired body x-axis, is the vector triple product $\hat{\mathbf{b}}^I_{x,d} = (\hat{\mathbf{b}}^I_{z,d} \times \hat{\mathbf{s}}^I_d) \times \hat{\mathbf{b}}^I_{z,d}$. However, this was experimentally found to result in yaw rotations such that the ground footprint of the slit is not

TABLE I: Overview of the six agile capture modes.

Category	Mode	Motivation	Section	Figure
Standard Imaging	0-Baseline	Conventional non-agile mode	III-C	3
Optical Enhancement	1-Slewing	Increase SNR	III-D	4
Coverage Enhancement	2-Multi-target	Observe multiple close-by targets	III-E	5
Optical Enhancement	3-Multi-angle	Increase SNR	III-F	6
Coverage Enhancement	4-Wide Swath	Extend across track coverage	III-G	7
Low latency	5-On-board-processing	Fast availability of information	III-H	8
Coverage Enhancement	6-Dynamic-pointing	Follow curved geospatial features	III-I	9

oriented perpendicular to the desired scanning direction. An alternative solution to determine the desired body x-axis to solve this issue is as follows. The body frame x-axis $\hat{\mathbf{b}}^I_{x,d}$ shall lie in the plane defined by the scanning direction and nadir. In other words, $\hat{\mathbf{b}}^I_{x,d}$ is a linear combination of $\hat{\mathbf{s}}^I_d$ and $\hat{\mathbf{l}}^I_z$,

$$\hat{\mathbf{b}}^I_{x,d} = a\hat{\mathbf{s}}^I_d + b\hat{\mathbf{l}}^I_z$$

The factors a and b are computed using the constraints of normality $||\hat{\mathbf{b}}^I_{x,d}|| = 1$, and orthogonality to the body z-axis $\hat{\mathbf{b}}^I_{x,d} \cdot \hat{\mathbf{b}}^I_{z,d} = 0$. This results in the following expressions for a and b

$$a = \frac{\pm 1}{\sqrt{1 + \left(\frac{\hat{\mathbf{s}}^I_d \cdot \hat{\mathbf{b}}^I_{z,d}}{\hat{\mathbf{l}}^I_z \cdot \hat{\mathbf{b}}^I_{z,d}}\right)^2}}, \tag{12}$$

$$b = \pm\sqrt{1 - a^2}, \tag{13}$$

where the sign of a is chosen first (before b), and can be either positive or negative depending on desired slit orientation being forward or backward. The sign of b is chosen to fulfill the orthogonality constraint.

This section has described a method to determine the a desired instantaneous pointing attitude $\mathbf{q}^L_B$ as a function of a given satellite position $\mathbf{p}^I$ and velocity $\mathbf{v}^I$, target location $\mathbf{T}^I$, and scanning direction $\hat{\mathbf{s}}^I_d$.

The satellite position and velocity vectors are time dependent and are determined from the satellite's TLE at time t, $[\mathbf{p}^I(t), \mathbf{v}^I(t)] = \mathrm{TLE}(t)$. The target coordinates are also time-dependent due to Earth's rotation $\mathbf{T}^I = \mathbf{T}^I(t)$. The desired scanning direction may also be a function of time $\hat{\mathbf{s}}^I_d(t)$.

We determine the satellite position and velocity vectors, and the inertial frame coordinates of the target coordinates using the orbital propagator and other functions in the python package Skyfield [44].

The attitude quaternion $\mathbf{q}^L_B(t)$ is estimated on-board via the satellite's ADCS subsystem. We quantify pointing performance by the following distance metric on SO(3) [45]

$$\gamma_{dev}(t) = \arccos\left(\left|\mathbf{q}^L_{B,d}(t) \cdot \mathbf{q}^L_B(t)\right|\right), \tag{14}$$

which computes the angular deviation or error between the two quaternions $\mathbf{q}^L_{B,d}(t)$ and $\mathbf{q}^L_B(t)$. This metric is chosen due to the clear physical meaning of γ_{dev}. For example, if the angular deviation γ_{dev} between two quaternions $\mathbf{q}_1$ and $\mathbf{q}_2$ is 5°, then the angle between two vectors formed by rotating the same vector with the two quaternions $\mathbf{q}_1$ and $\mathbf{q}_2$ is 5°. If one quaternion is a desired reference attitude, and the other is the actual obtained attitude, then the attitude was 5° off.

B. Capture modes

In this subsection, the six imaging modes that exploit agile attitude control and push-broom imaging are presented. Section III-C describes the baseline, non-agile imaging mode. The agile imaging modes are described in Section III-D to Section III-I. See Table I for an overview. Capture mode 1-Slewing in Section III-D is for improved GSD and SNR. Capture mode 2-Multi-target in Section III-E describes agile pointing to scan two targets that lie close to each other in a single pass, which can not be observed with a single scan. The capture modes in Section III-F and Section III-G (modes 3-Multi-angle and 4-Wide-swath) are designed to improve data collection from a single target location by scanning multiple times during a single pass. Section III-H describes capture mode 5-On-board-processing for fast downlink of processed data from observation to a ground station using on-board processing. Capture mode 6-Dynamic-pointing in Section III-I is for arbitrary curved scanning directions, e.g. for scanning along a coastline. The capture modes in Section III-D and Section III-I are SA-EOS-type modes.

The modes improve the collected data in three ways: i) by optical enhancement (modes 1-Slewing and 3-Multi-angle); ii) by coverage enhancements (modes 2-Multi-target, 4-Wide Swath and 6-Dynamic-pointing); and iii) by reducing ground availability latency (mode 5-On-board-processing).

This is how the capture modes relate to the agile EOS scheduling problem. The unit of the agile EOS scheduling problem are straight line image strips with arbitrary orientation. A scheduling algorithm generates a list of sequential image strips to cover point and polygon targets. Thus capture mode 2-Multi-target would be scheduled naturally using the method when the input is two close-by lying point targets. Similar with 4-Wide-swath. The capture modes 5-On-board-processing, 3-Multi-angle and 6-Dynamic-pointing could be integrated as different atomic tasks into a agile EOS scheduling system. By suitably parameterizing the modes, the target list could be augmented with special coverage and SNR requirements, and the scheduling algorithm would pick from a list of suitable imaging modes to schedule.

Each capture mode is presented with a qualitative figure illustrating the sequence of actions performed by the satellite. See, for example, Figure 3. The arrow represents an attitude change action between points in time t_{-1} and t_0. The swaths at t_0 and t_1 and the dashed lines connecting them represent push-broom imaging.

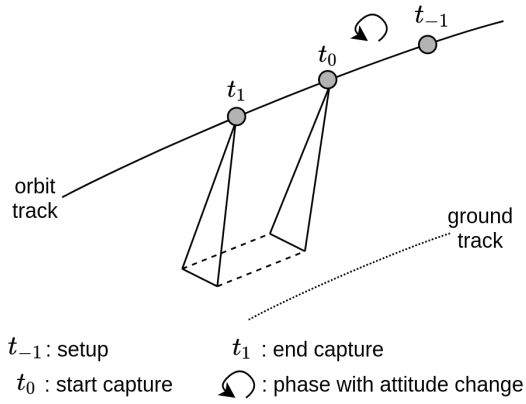

Fig. 3: Baseline capture mode that does not require agile attitude control.

C. Capture mode 0-Baseline

Push-broom EOS can scan a target area by utilizing the satellite's orbital motion to move the sensor FoV across the target. This is the baseline push-broom capture mode illustrated in Figure 3. This mode consists of two phases. The first phase is performed during the time interval from t_{-1} to t_0. During this phase, on-board preparations are done, and the satellite rotates into the desired attitude before scanning the pre-selected target area. The pointing attitude consists of a single rotation around the LVLH x-axis by a roll angle φ to center the target location inside the sensor's FoV. There is no need for pointing ahead or back, as this would only increase the distance to the target and decrease the satellite elevation angle during scanning. Thus, this is a non-agile imaging mode. Scanning happens during the second phase, which is the time between t_0 and t_1.

The quaternion describing the desired attitude of the body frame with respect to the LVLH frame is computed as

$$\mathbf{q}_{B,d}^{L} = \left[\cos\frac{\varphi}{2}, \sin\frac{\varphi}{2}, 0, 0\right]^{\top}. \tag{15}$$

The length of the scanned area d is

$$d = v(t_1 - t_0)\frac{R_e}{R_e + h} + \delta(l_s, \varphi) \tag{16}$$

where $\delta(l_s, \varphi)$ is a (small) additional distance due to the width of the instantaneous point-spread function in the along track direction l_s and off-nadir angle φ, and v is the speed along the ground track.

Using capture mode 0-Baseline, coverage is limited to sequential image strips. For multiple targets that do not lie in on a line parallel with the satellite ground track, the satellite needs time for pointing before recording the next image strip. The minimum along-track distance L_{min} between the strips can be approximated as follows

$$L_{min} = vT_m = v\frac{\Delta\gamma}{\omega_{max}} \tag{17}$$

where v is the satellite orbital speed, $\Delta\gamma$ is the required angular change to point to the next target, ω_{max} is the maximum rate of change that the satellite can rotate with, and T_m is the time required for the attitude change. According to this approximation, the larger the difference in off-nadir angle between two targets, the longer is the time required for the attitude change and the larger must be the along-track distance between the targets need to be for the possibility of imaging both.

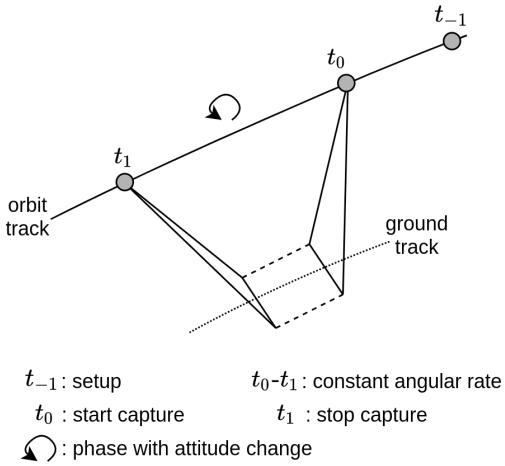

Fig. 4: Capture mode 1-Slewing.

D. Capture mode 1-Slewing

Capture mode 1-Slewing, also called pitch motion compensation, is using control of the angular velocity to influence the along track GSD and overlap of successive scan lines, see Figure 4. This can increase SNR by collecting more light from a smaller area. This mode is described in detail in [38], and attitude control and GSD results are presented in [11].

Mode 1-Slewing is modelled differently from the other modes, because the HYPSO-1 ADCS subsystem was using a different control mode, which is constant attitude rate control, instead of pointing control. However, we note that mode 1-Slewing may be realized using the method from Section III by defining a suitable ground path. The mode 1-Slewing is modelled as follows. An initial look ahead angle β_1 and a final look back angle β_2 as well as a duration T_{sl} is chosen. The angles can be chosen symmetrically, $\beta_1 = -\beta_2$, but they do not need to. The angular velocity is then derived from the angular difference and the duration $(\beta_2 - \beta_1)/T_{sl}$. The duration can be chosen with some relationship to the capture scanning duration.

According to [38], binning by factor N improves the SNR by $\sqrt{N}$. If the angles β_1 and β_2 are chosen such that along track coverage, i.e., scan length, is halved, then the data can be binned by factor 2 in the scanning direction to obtain the same spatial resolution as a 0-Baseline capture, increasing the SNR. For a point target, the user may specify in addition either, i) a desired SNR increase factor; or ii) an maximally acceptable reduction factor in scan length. The angles β_1 and β_2 can then be chosen to to fulfil either of these specifications, obtaining the increase in SNR.

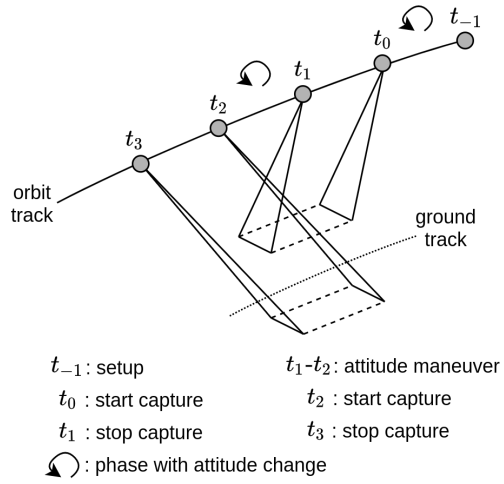

Fig. 5: Capture mode 2-Multi-target scans two targets within a single pass. It is designed to record data from multiple targets that lie too close to each other to be scanned with non-agile pointing.

E. Capture mode 2-Multi-target

With capture mode 2-Multi-target, two or more target areas can be observed that lie too far away from each other to be covered with a single scan. See Figure 5 for an illustration of this capture mode. Recording images in this way is similar to how imaging is assumed to be done in the previous research solving the agile imaging scheduling problem.

The maneuver consists of four phases, see Figure 6

1) Phase one consist of preparations and is performed from time t_{-1} until time t_0. Similar to phase one in capture mode 0-Baseline, setup and initial pointing is done.
2) Phase two consists of imaging and constant attitude pointing with respect to LVLH-frame and happens between t_0 and t_1.
3) During phase three between time t_1 and time t_2, the attitude setpoint is changed to setup pointing for the second scan.
4) Lastly, phase four consists again of imaging and constant pointing between time t_2 and time t_3.

The procedure described in Section III-A to compute an attitude quaternion requires four inputs, which are target coordinates, scanning direction, satellite TLE and a timestamp, all of which are given, except the timestamp. The timestamp is computed as follows. Let the times at which the satellite culminates (reaching highest elevation) over the two targets be t_{c1} and t_{c2}, which can be derived from the target locations and the satellite TLE. We compute the mean culmination time $t_c = (t_{c1} + t_{c2})/2$, serving as the reference point of the maneuver. The time required for the attitude change maneuver, $t_2 - t_1 = T_m$ is chosen depending on satellite capabilities. The scan durations for the first and second scan are respectively $T_{s1} = t_1 - t_0$ and $T_{s2} = t_3 - t_2$. The timestamps t_{d1} and t_{d2} for computing the quaternions $\mathbf{q}^L_{B,d,1}$ and $\mathbf{q}^L_{B,d,2}$ for both pointing phases are then determined as follows

$$t_{d1} = t_c - \frac{T_m}{2} - \frac{T_{s1}}{2}, \tag{18}$$

$$t_{d2} = t_c + \frac{T_m}{2} + \frac{T_{s2}}{2}. \tag{19}$$

This mode can simplify the agile imaging scheduling problem by switching from a baseline atomic task to this task, when two successive targets to not satisfy the constraint given in (17).

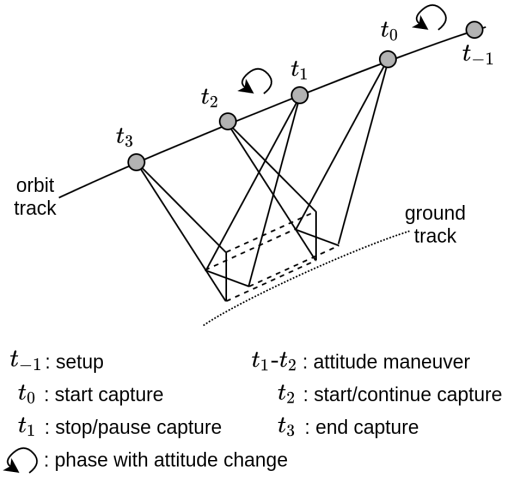

Fig. 6: Capture mode 3-Multi-angle imaging.

F. Capture mode 3-Multi-angle

Multiple image scans are acquired by pointing ahead and back along track in a single pass.

Capture mode 3-Multi-angle could, for example, be used for one or more of the following four applications: i) improving SNR; ii) improving spatial resolution; iii) adapting the exposure time in the second image depending on the first, e.g., to optimize exposure or dynamic range; and iv) informing atmospheric correction methods. All four applications rely on specific post processing methods. Only i) is investigated in this paper.

The desired attitude quaternions for pointing to the target are computed similarly as in the previous mode 2-Multi-target, except that the culmination times and the scan durations are be equal: $t_{c1} = t_{c2} = t_c$ and $T_{s1} = T_{s2} = T_s$. The attitude quaternions $\mathbf{q}^L_{B,d,1}$ and $\mathbf{q}^L_{B,d,2}$ are then determined using the following timestamps

$$t_{d1} = t_c - \frac{T_m}{2} - \frac{T_s}{2}, \tag{20}$$

$$t_{d2} = t_c + \frac{T_m}{2} + \frac{T_s}{2}. \tag{21}$$

Choosing the timestamps in this way makes the maneuver symmetric both in space around the culmination point at time t_c. Specifically, both image scans will have the same elevation angle.

The user may flag a point target for multi-angle imaging, such that the agile imaging scheduling problem uses a multi angle atomic task instead of the baseline atomic task.

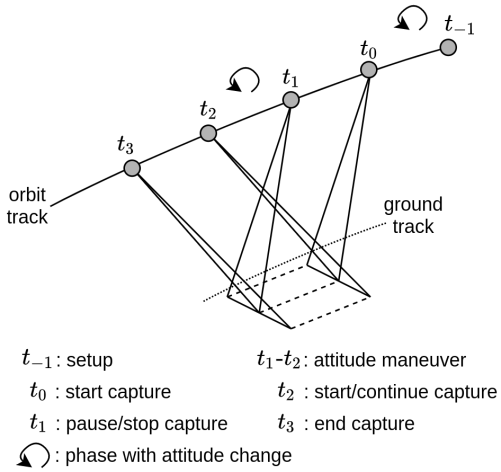

Fig. 7: Capture mode 4-Wide Swath to extend across track coverage of a target during a single pass.

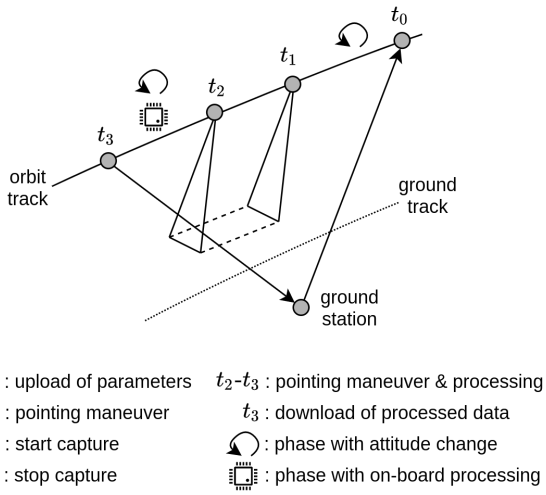

Fig. 8: Low latency data acquisition mode 5-On-board-processing.

G. Capture mode 4-Wide Swath

Capture mode 4-Wide-swath, illustrated in Figure 7, extends the across track coverage of a satellite by sequentially pointing and scanning positively and negatively in the across track direction with respect to a target location.

This mode is similar to capture mode 3-Multi-angle, as it consists of two scans over a single target location and the maneuver is assumed to be symmetric about the culmination timestamp. The timestamps used in determining the pointing quaternions $\mathbf{q}^L_{B,d,1}$ and $\mathbf{q}^L_{B,d,2}$ are determined identically as in mode 3-Multi-angle.

This capture mode differs from 3-Multi-angle by adding adjusting the pointing quaternions $\mathbf{q}^L_{B,d,1}$ and $\mathbf{q}^L_{B,d,2}$ with small positive and negative roll rotations $\pm\alpha$ as follows

$$\mathbf{q}^{L'}_{B,d,i} = \mathbf{q}^L_{B,d,i} \otimes \left[\cos\frac{\alpha}{2}, (-1)^i \sin\frac{\alpha}{2}, 0, 0\right]. \qquad (22)$$

The angle α may be set to slightly less than half the across track field of view of the push broom camera, in order to facilitate some overlap and prevent a gap in case of attitude control inaccuracies.

A similar mode as this one has been demonstrated in the Agile MicroSat, although using a snapshot camera [16], [17].

Similar to 3-Multi-angle, The user may flag a point target for wider coverage, such that the agile imaging scheduling problem uses a wide-swath atomic task instead of the baseline atomic task.

H. Capture mode 5-On-board-processing

Using capture mode 5-On-board-processing, data latency can be reduced to just minutes. The mode is initiated after ground station contact with task parameter upload until time t_0, as illustrated in Figure 8. This capture mode is performed in four phases:

1) During phase one, the satellite rotates to point to the specified target location until time t_1.
2) Phase two consists of image scan acquisition from t_1 to t_2.
3) Phase three consists of internal data handling and on-board processing while the satellite rotates to point back to a ground station between t_2 and t_3.
4) In phase four the data is downlinked, after on-board processing is completed.

These phases require that both the target and the ground station is in viewing range during the time of the maneuver. Only in that case data latency can be maximally reduced. No target or ground station proximity increases the latency compared to the ideal case.

This mode is also dependent on suitable on-board processing algorithms that have a short enough execution time, such as the sparse SVM classification presented in Røysland et al. [37]. Therein, the classification was performed on-board as a technology demonstration. The same algorithm is used in this work as part of capture mode 5-On-board-processing to achieve low latency data availability on-ground.

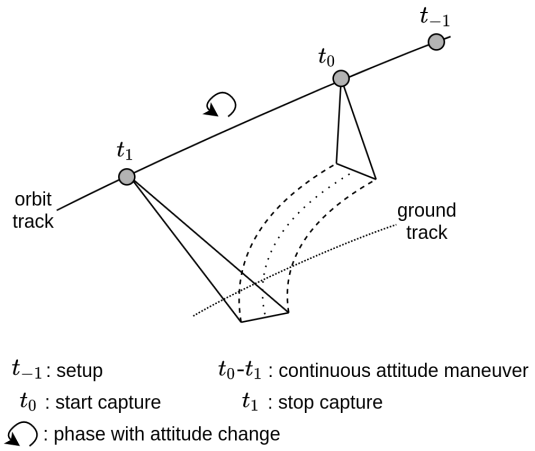

Fig. 9: Capture mode 6-Dynamic-pointing for agile scanning

I. Capture mode 6-Dynamic-pointing

Capture mode 6-Dynamic-pointing is illustrated in Figure 9. The mode is defined by a parametric ground path in longitude $\lambda(p)$ and latitude $\phi(p)$ with either time or distance as parameter p. The scanning direction is determined from the tangent vector of the target position. If time is the parameter, one may define a total scan duration T_s for which the ground path shall be followed while staying inside angular velocity and angular acceleration constraints of the satellite. The path is converted to a discrete quaternion sequence using a discretization time interval Δt. No matter whether the path is defined in terms of time or distance, the path is discretized into M points, that are uniformly with respect to time. For each sample at time $t_m = t_0 + m\Delta t$, $m \in \{0, 1, ..., M-1\}$, the longitude and latitude determine the target location $\mathbf{T}^I(\lambda(t_m), \phi(t_m))$. The scanning direction is given by the tangent vector of the path $\hat{\mathbf{s}}_d^I(t_m) = \frac{\mathrm{d}\mathbf{T}^I}{\mathrm{d}t}(t_m)$. Thus the pointing quaternion can be computed using the procedure outlines in Section III-A.

The recording frame rate f_r and the total number of lines to record N are chosen to match the maneuver duration, i.e., $T_s = N/f_r$.

In order to prepare for quaternion sequence pointing, a *running start* is generated consisting of quaternions corresponding to a given duration, which is 30 seconds in our experiments. This is done by finding the difference quaternion $\tilde{\mathbf{q}}$ between the first two quaternions in the sequence

$$\tilde{\mathbf{q}} = \mathbf{q}_{B,d}^L(t_1) \otimes \bar{\mathbf{q}}_{B,d}^L(t_0) \tag{23}$$

where $\bar{\mathbf{q}}$ denotes quaternion conjugation of $\mathbf{q}$. Using the difference quaternion, the attitude is extrapolated from the first quaternion in the maneuver for a short period before the start of the scanning maneuver.

$$\mathbf{q}_{B,d}^L(t_i) = \bar{\tilde{\mathbf{q}}} \otimes \mathbf{q}_{B,d}^L(t_{i+1}) \tag{24}$$

for $i \in \{-K, ..., -2, -1\}$.

Capture mode 6-Dynamic-pointing could be used to cover two closely located targets similar to mode 2-Multi-target. Thus 6-Dynamic-pointing could in some cases be used instead of the 2-Multi-target mode.

If the user provides a path or some other description of a long target that cannot be covered with along track scanning, the 6-Dynamic-pointing capture mode can replace the baseline imaging atomic task when solving the agile imaging scheduling problem.

Satellite attitude motion during imaging may cause issues related to motion blur. In general, to reduce motion blur in images, the angular rate of the instrument should be small enough such that the angular change during a single image exposure or integration time is less than the angular extent of a sensor pixel. For push-broom instruments, there is a difference in how motion blur forms in an image due to angular motion. Perpendicular to the scan direction the rule of keeping the angular motion during exposure less than the angular extent of a pixel applies. Along the scan direction, motion is required to form an image and the angular speed influences resolution and coverage.

IV. Experimental Setup

A. HYPSO-1

HYPSO-1 [38], [39] is primarily a science-driven mission collecting ocean color data, as well as a test platform for novel operational concepts, onboard data processing, operational procedures, and planning methods. In addition to agile pointing, the operational concepts include the use of onboard data processing with low-latency delivery of data for real-use, e.g. guiding an autonomous surface vehicle, or time-critical harmful algal bloom warning [46]. Thus, HYPSO-1 can be a part of a system-of-systems that includes in-situ marine robots and unmanned aerial systems [47].

HYPSO-1 is a small satellite based on COTS components. It consists of a 6U satellite bus from Kongsberg NanoAvionics with an in-house developed hyperspectral push-broom camera payload. The hyperspectral camera can be configured with a capture data rate of up to 200 Mbit/s. With a downlink capacity of 1 Mbit/s using its S-band radio and a single ground station on Svalbard, data downlink is limited to about 400 MB of data per day. Operations outside of ground station contact are scheduled using scripts that send sequences of data packets onto the satellite message bus at specified points in time. The scripts are in the form of ASCII text files and resemble shell scripts. Continuous recording is limited to about 150 MB at a time, before on-board memory is full and recording needs to be paused for processing. Processing can take anywhere from about 20 seconds to 7 minutes depending on recording parameters. This time may be longer depending on if and which additional on-board processing is performed. After processing, recording can be resumed. HYPSO-1 was launched into a circular sun-synchronous orbit with a semi-major axis altitude of about 530 km in January 2022. As of October 2024, the semi-major axis altitude has decayed to 475 km, changing the full swatch width and GSD respectively from about 74 km and 62 m to about 67 km and 56 m. The HYPSO-1 hyperspectral imager is a transmission grating design with a FoV of 8.0 degrees. The hyperspectral data cube configuration in terms of lines, samples and bands is freely configurable, with a nominal configuration being 956 lines,

684 samples and 120 bands. Sometimes a configuration of 598 lines, 1092 samples and 120 bands is also used. With a configuration of 684 samples, the swath width is 39 km, and with a configuration of 1092 samples, the swath width is 62 km. The maximum line or frame rate is 22 Frames Per Second (fps) at 684 samples and 12 fps at 1092 samples and can be set lower if desired. The along track GSD is about 320 m at 22 fps while nadir pointing. The sensitive spectral range is 400 to 800 nm with spectral sampling of about 0.37 nm. The data is binned in the spectral dimension to obtain 120 bands and an effective Full Width Half Maximum (FWHM) of about 3.3 nm. See Table II for a summary of key specifications for the HYPSO-1 satellite and hyperspectral imager.

TABLE II: Specifications of the HYPSO-1.

Property	Value
Spectrometer design	Transmission grating
FoV	8.0°
Altitude at launch	530 km
Altitude as of October 2024	475 km
Swath width at nadir	74 km @ 530km, 67 km @ 475 km
GSD at nadir	62 m @ 530 km, 56 m @ 470 km
Spectral range	400 - 800 nm
Bands	120
Samples along the slit	684, 1092
Frame rate	$\in$ [1, 22] fps
Along track GSD at nadir	ca. 320 m

B. Planning

The duration of a data acquisition of nominal dimensions with 956 frames at a framerate of 22 fps is 43.44s. The capture mode 1-Slewing is planned with $\beta_1 = -\beta_2 = 10°$ over $T_{sl} =$ 43.44s, giving an angular velocity of 0.46 $°/$s. This is chosen to decrease the GSD by approximately 3 times compared to capture mode 0-Baseline.

Due to their similarity in terms of phases that they consist of, the planned parameters of modes 3-Multi-angle, 4-Wide-swath, and 2-Multi-target are presented together in Table III. For modes 3-Multi-angle and 4-Wide-swath, to reduce the look-ahead and -back off-nadir angle, the scan duration is shortened by reducing the total number of frames down to around 300. Maneuvering duration T_m has been set to a preliminary long value of around one minute. For capture mode 2-Multi-target, the two captures' frame rate and frame count are chosen differently to utilize fast Field Programmable Array Gate (FPGA) image compression during the first capture, which requires dimensions 956 frames by 684 samples by 120 bands. The second capture uses cube dimensions for higher swath width (1092 samples), which requires a lower frame rate and frame count (see Table III) and time-consuming software-based data compression.

Capture mode 5-On-board-processing was set up by uploading the necessary files for performing on-board classification and waiting for a suitable ground station pass. The chosen pass was on a summer evening on 2023-07-09 over Norway, still exhibiting daylight, although with a low sun angle. The upload and execution of the script for this mode were scheduled at the start of the pass. The script contained commands for satellite pointing, payload power control, data collection, and lastly, performing on-board classification. The progress of the script is monitored during the pass, and once the script is finished, a command for downloading the classified image file is send.

An example of capture mode 6-Dynamic-pointing was planned for date 2023-08-29. The parametric ground path is defined to follow along the Marajó Bay and Pará River, near the city of Belem in Brazil.

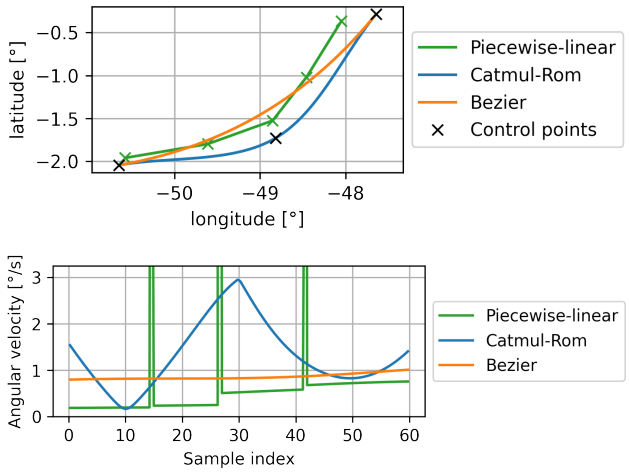

Fig. 10: Top: Three paths defined to follow the Pará River. Both the Catmul-Rom spline and the Bézier curve use the control points marked with black x's. The piece-wise linear path uses the control points marked with blue x's. Bottom: Plot showing the required angular velocity for a satellite following the three paths with the specific orbit of HYPSO-1 when passing over the location on the day 2023-08-29.

The ground path is generated by interpolating control points. Figure 10 shows a comparison of three curves that were considered for the maneuver. The piecewise linear curve is included because it was the first type that was generated for debugging the method. The other two curves are a quadratic Bézier curve, and a Catmul-Rom spline. Figure 10 also shows the corresponding angular rate required to follow these paths. The curves generated by Catmul-Rom splines pass though the control points that define the spline, which is called the interpolating property. The locations of the control points were manually set to satisfy an angular velocity constraint of less than $1°/$s while still following the shape of the river. The $1°/$s limitation is given by the ADCS subsystem provider Kongsberg NanoAvionics.

A Catmul-Rom spline is easier to design intuitively due to the interpolating property. But this property is also the cause of generating curves with a larger curvature. The higher curvature of the Catmul-Rom spline leads to large yaw rotations that violate the $1°/$s requirement. Thus, the path chosen for the maneuver is the quadratic Bézier curve defined by three control points denoted with black crosses in Figure 10.

A framerate of 16 fps and nominal cube dimensions are chosen, specifically, 956 lines are to be recorded, resulting in a total imaging duration of 59.75 seconds. The curve is discretized according to the 4 Hz sample rate of the ADCS system on the satellite. Hence, the curve is sampled

TABLE III: Choice of parameters for three of the the presented capture modes.

Parameter	Value capture mode 2-Multi-target	Value capture mode 3-Multi-angle	Value capture mode 4-Wide Swath
f_r	22 Hz and 11.5 Hz	12 Hz	12 Hz
N	956 and 585	300	315 (282)
T_s	43.25 s and 50.87 s	25 s	26.25 s
T_m	55 s	55 s	60 s
$\mathbf{q}^L_{B,d,1}$	[0.960420, -0.185223, 0.204299, 0.039341]	[0.952934, 0.163179, 0.251860, -0.043085]	[0.963864, 0.0, 0.266396, 0.0]
$\mathbf{q}^L_{B,d,2}$	[0.965942, -0.097941, -0.238283, -0.024187]	[0.962213, 0.132244, -0.235806, 0.032466]	[0.962774, -0.051308, -0.265392, -0.0]
t_{-1}	2023-08-31 15:36:34	2023-08-08 17:25:21	2023-07-13 07:01:48
t_0	2023-08-31 15:40:49	2023-08-08 17:27:25	2023-07-13 07:08:07
t_{d1}	2023-08-31 15:41:11	2023-08-08 17:27:38	2023-07-13 07:08:21
t_1	2023-08-31 15:41:33	2023-08-08 17:27:50	2023-07-13 07:08:34
t_c	2023-08-31 15:42:00	2023-08-08 17:28:18	2023-07-13 07:09:04
t_2	2023-08-31 15:42:28	2023-08-08 17:28:45	2023-07-13 07:09:34
t_{d2}	2023-08-31 15:42:53	2023-08-08 17:28:58	2023-07-13 07:09:48
t_3	2023-08-31 15:43:18	2023-08-08 17:29:10	2023-07-13 07:10:01

at $\frac{59.75\text{ s}}{0.25\text{ s}} = 239$ equidistant locations. Applying the satellite pointing method described in Section III-A to each location sample yields the quaternion time series shown in the top plot of Figure 11. For ease of interpretation, an equivalent Euler angle time series is shown in the middle plot of Figure 11. The bottom plot of Figure 11 shows the target curve relative to the satellite's ground track during the time of the maneuver. The quaternion time series and the script for the maneuver and simultaneous imaging uploaded to the satellite prior to the maneuver.

V. Results and Discussion

The following subsections present the results from planning and performing all these agile modes on HYPSO-1.

A. Capture mode 1-Slewing results

Four 1-Slewing images are presented here, see Table IV. The "Gloria" scene has a baseline capture associated with it, called "Gloria non-slew" in Table IV. The "Gloria" scene is near the Danube delta in the Black Sea. The "Bohai" scene is over the chinese city Weihai in the Yellow Sea. The "Patras" scene covers the greek cities Corinth and Tripoli. Lastly, the "Railroad" scene is of the Railroad Valley in Nevada, which hosts a calibration site for remote sensing. See Figure 12 for Red Green Blue (RGB) composites of the corresponding slew and non-slew images and see Figure 13 for the other three images. The SNR is computed for all five images and compared. The chosen SNR estimation method requires a contiguous set of pixels over a uniform scene. As part of the SNR estimation, the noise level in the data is determined by analyzing the variation in signal within the set of pixels. The number of pixels used for SNR estimation should be as large as possible to be statistically significant but should not contain too much spatial variation. The sets of pixels of the images used for SNR estimation are marked with gray rectangles in Figure 12 and Figure 13. Before computing SNR, the slew images are binned in the along track direction by a factor of 3, corresponding to the 3 times reduction in GSD achieved via slewing. Thus, we expect the SNR of the slew image to be around $\sqrt{3} \approx 1.73$ higher. This also corresponds to a 3 times reduction in image length in the scan direction. Estimation of SNR from the image data makes the results presented here different from [11] and [12].

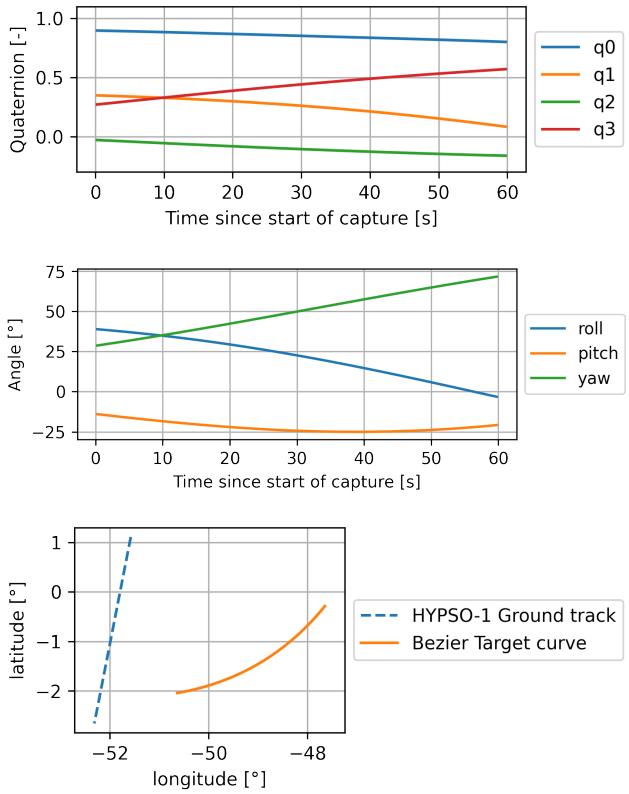

Fig. 11: Top: The resulting quaternion sequence relative to LVLH frame that was uploaded to HYPSO-1. q0 is the scalar part of the quaternion. q1, q2, and q3 form the vector part. Middle: The quaternion sequence converted to euler angles referenced to LVLH frame. Bottom: Plot showing the HYPSO-1 ground track during the maneuver together with the Bézier path. Satellite motion is north to south.

The slew images are considerably blurrier than the non-slew images due to overlapping of the point-spread function between successive line scans. The width of the instantaneous point-spread function in the along track direction of the HYPSO-1 instrument is about 520 m, while the GSD is reduced from about 321 m to about 117 m by slewing [11]. The diminishing along track resolution gain in a push-broom instrument by reduction of GSD is investigated in [48].

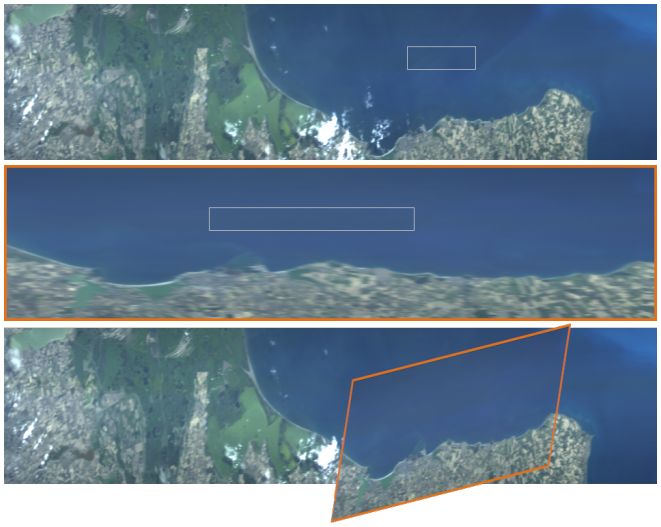

Fig. 12: Raw data RGB composites of the baseline non-slew (top) and slew (middle) image of the Gloria target. The gray rectangles represent the area used for SNR estimation. In the bottom image, the slew image has been referenced and overlain into the non-slew image. The border of the slew image is highlighted with orange.

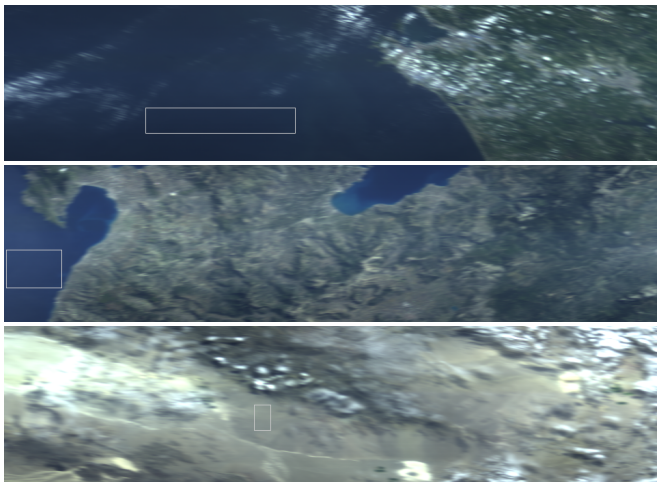

Fig. 13: Raw data RGB composites of the other three slew images. Top: Bohai. Middle: Patras. Bottom: Railroad.

We estimate SNR in the same way as in [39], which consists of two methods for estimating SNR empirically from a dataset. The method computes a spatial and a spectral SNR. The estimated spatial and spectral SNR per band for the images in Table IV are shown in Figure 14.

The estimated SNR for the Gloria slew scene is about 1.89 times higher spatially on average across all bands and 1.79 times higher spectrally on average across all bands, roughly in line with expectation. Thus, capture mode 1-Slewing is achieving a higher SNR than the baseline maneuver at the expense of coverage.

TABLE IV: Overview of the slew maneuvers

Scene	Date [UTC]	Exp. [ms]	Mean Std. dev.
Gloria	2022-07-24 08:30	30	162
Bohai	2022-07-24 02:11	20	184
Patras	2022-10-10 08:51	35	304
Railroad	2022-07-24 18:03	20	474
Gloria non-slew	2022-07-16 08:29	30	101

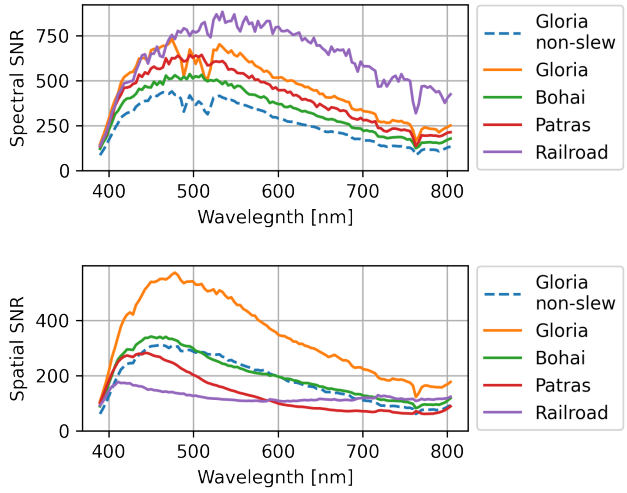

Fig. 14: Spectral (top) and spatial (bottom) SNR for the scenes in Table IV. The dashed line indicates the non-slew image.

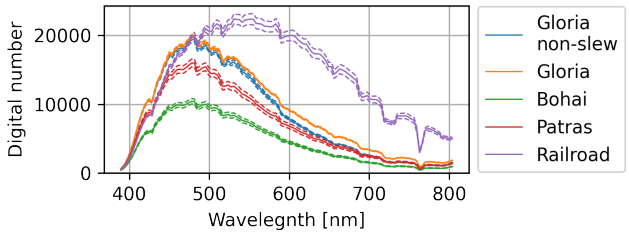

Fig. 15: The mean signal level over the pixels of a scene used in SNR estimation.

Figure 15 shows the mean spectrum across the region considered for the images and 1-σ deviation per band. The mean deviation for each scene across bands and the exposure time used during recording is shown in Table IV. Considering the SNR in Figure 14 and the signal level statistics in Figure 15, we can see that spectral SNR is correlated with signal level and that even though the Patras scene had the highest exposure time, its signal level is less than the Gloria scene, which is explained by that the image was taken in October, as opposed to July, meaning lower sun angles and thus less reflected light causing less received signal by HYPSO-1. The slew and non-slew Gloria scenes are comparable, because they were captured using the same exposure time and they have similar sun angles. The sun angles are similar, because they were captured at similar times of year and HYPSO-1 is in a sun-synchronous orbit.

The standard deviations for the Patras and the Railroad scenes are 304 and 474 digital counts, respectively. This relatively high spatial variation compared to the other slew scenes is likely due to variation in the scene. This violates the assumption a uniform scene for a good spatial SNR estimation.

However, no large contiguous area is spatially uniform in the Patras and Railroad Valley scenes, leading to high signal variance. Due to the high signal variance, the amount of noise in the scenes could be overestimated, leading to a lower estimate of spatial SNR in Figure 14.

B. Capture modes 2-Multi-target, 3-Multi-angle and 4-Wide Swath results

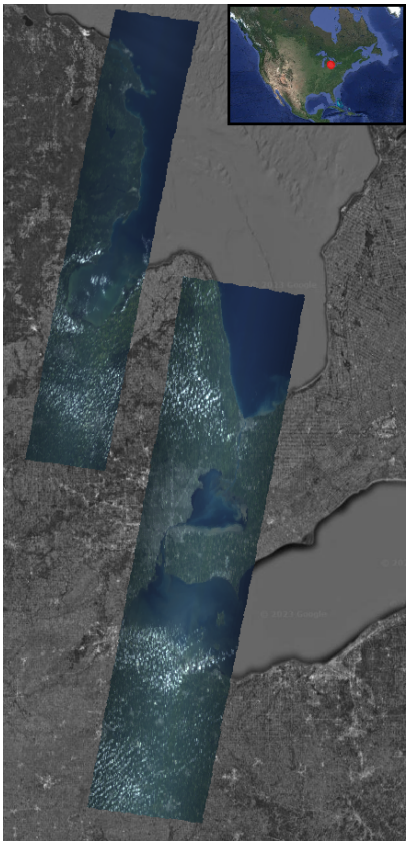

Fig. 16: Image showing raw data (uncalibrated) RGB composite of the two sequentially acquired images. Both the Saginaw Bay of Lake Huron, and the west side of Lake Erie were recorded during a single pass. (Background imagery ©Google Maps, ©TerraMetrics)

The resulting images from performing capture modes 2-Multi-target, 3-Multi-angle and 4-Wide Swath are shown in Figure 17, Figure 18 and Figure 16, respectively.

Figure 16 shows the two images acquired during the 2-Multi-target capture maneuver. The images are uncalibrated raw data RGB composites and are manually georeferenced. The image acquired first while pointing ahead was to the west and shows the Saginaw Bay of Lake Huron. The second image acquired last while pointing back is shown to the east and is of Lake Erie. The data shows that agile pointing enables imaging of targets that overlap in the along track direction. The difference in swath width of the two images in Figure 16 is due to different imaging configurations. The first image as configured with nominal dimensions, specifically 684 samples, while the second image was configured with 1092 samples.

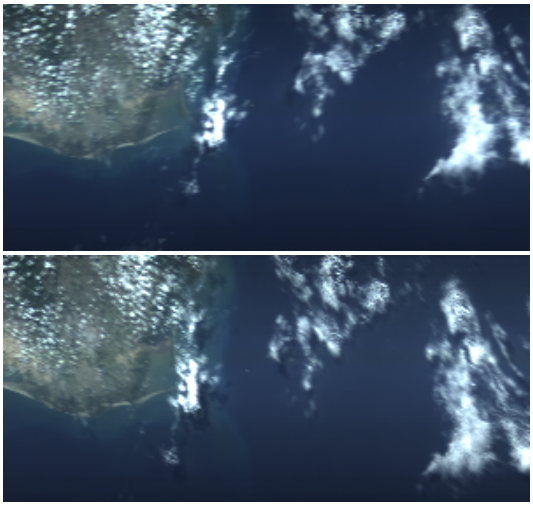

Fig. 17: Uncalibrated raw data RGB composite of the 3-Multi-angle imaging mode performed on 2023-08-08. Top image was scanned from 17:27:25 UTC to 17:27:50 UTC and the bottom image was scanned from 17:28:45 UTC to 17:29:10 UTC.

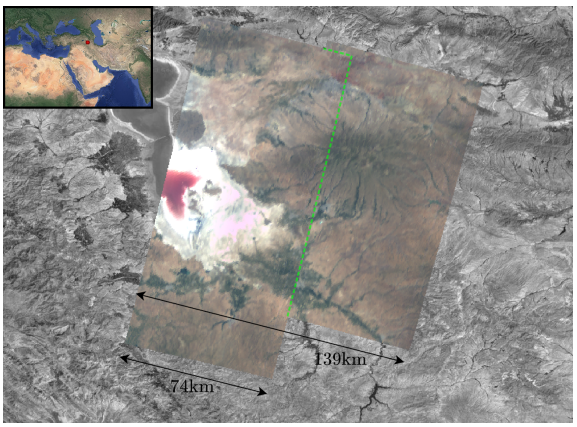

Fig. 18: Image showing the two successively acquired images during capture mode 4-Wide-swath. The green dashed line indicates the boundary of the second capture where it is overlapping the first capture. (Background imagery ©Google Maps, ©TerraMetrics)

Figure 17 shows two images of the same location acquired during the 3-Multi-angle capture mode. Cloud movement can be observed. Due to the geometric symmetry of the two captures, their off-nadir angles are similar, leading to a similar signal magnitude of the data. The SNR was estimated for both 3-Multi-angle acquisitions. Then, the images were manually spatially co-registered and stacked by adding spatially aligned pixels. The SNR was then estimated for the stacked image as well. The results are shown in Figure 19. The SNR estimate is on average 1.36 times larger spatially and 1.44 times larger spectrally compared to the first 3-Multi-angle acquisition. Thus, scanning the same area multiple times during the same pass can increase SNR compared to the baseline maneuver.

Figure 18 shows two radiance RGB composites of the images acquired during the 4-Wide Swath capture mode. The images were manually georeferenced by identifying ground

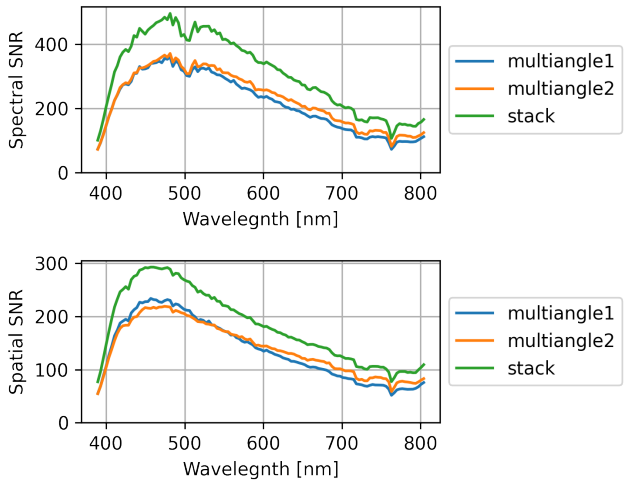

Fig. 19: Estimated SNR from the 3-Multi-angle acquisitions. Top: Spectral SNR. Bottom: Spatial SNR.

control points. A single, non-agile scan has a swath width of ca. 40km at nadir using nominal dimensions and ca. 70km using wide dimensions. For the recording shown here, wide dimensions were used. The swath-width of the resulting images was effectively increased from 74 km to 139 km, almost doubling what a baseline maneuver would achieve.

The attitude error for the three static pointing capture modes is computed using (14) and is shown in Figure 20. All three show a pointing error below 1 degree after almost 40 seconds, indicating that the choice of T_m of 55s or 60s is conservative and could be reduced to 40s.

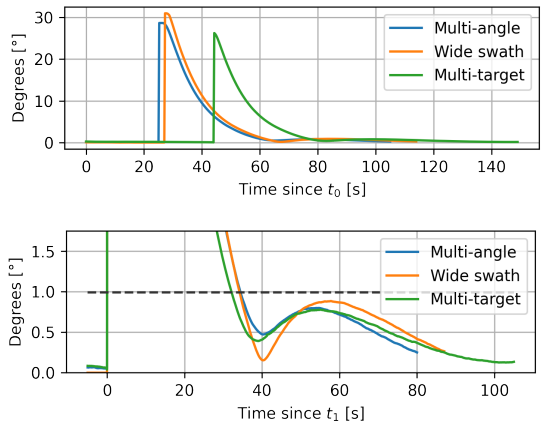

Fig. 20: Attitude error between the reference and the on-board estimated attitude. Top: Attitude error between times t_0 and t_3. Bottom: Attitude error between times t_1 and t_3.

C. Capture mode 5-On-board-processing results

Capture mode 5-On-board-processing results are shown in Figure 21. See Table V for an overview of the sequence of events.

TABLE V: Sequence of events during the 5-On-board-processing operation.

Date and Time [UTC]	Event
2023-07-09 18:55:51	Satellite Acquisition of Sight (AOS)
2023-07-09 18:57:47	Uplink of imaging parameters done
2023-07-09 18:57:57	Satellite begins pointing to target
2023-07-09 18:59:12	Payload boot up done
2023-07-09 18:59:45	**Image scan start**
2023-07-09 19:00:28	**Image scan end**
2023-07-09 19:00:31	Image stored to SD Card
2023-07-09 19:00:34	Compressed image stored to SD Card
2023-07-09 19:01:00	Image classification start
2023-07-09 19:01:09	Image classification end
2023-07-09 19:01:28	**Classified image downlinked**
2023-07-09 22:13:36	Hyperspectral data-cube fully downlinked

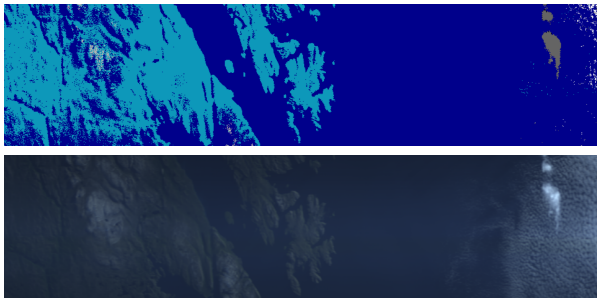

Fig. 21: Top: The segmented image that was downlinked minutes after the data was recorded. Bottom: Raw data RGB corresponding to the classified image that was downlinked 3 hours later.

This procedure demonstrates the feasibility of higher-level on-board processing to get low-latency information quickly from a space-borne platform, representing a substantial speedup in latency compared to the baseline maneuver.

D. Capture mode 6-Dynamic-pointing results

The data from a capture mode 6-Dynamic-pointing maneuver is shown in Figure 22. The image is manually georeferenced and shows an uncalibrated raw data RGB composites.

In addition to image data, Figure 22 also shows the planned path along which to scan. The imagery follows the planned path, which is not parallel to the satellite ground track, and thus required continuous dynamic pointing to follow. The data has a minor angular offset to the north-west with respect to the planned path. Possible explanations for this offset include attitude and calibration errors. Figure 22 also shows the coordinates of the control points for the quadratic Bézier curve that served as path to follow.

VI. Conclusion

Using the simple and modular agile push-broom imaging maneuver planning method that was presented here, we planned and executed several different agile push-broom imaging maneuvers, which generated data with advantages compared to non-agile imaging. The signal-to-noise ratio is increased by slewing or multi-angle imaging. On-board processing decreased data latency. Spatial coverage is expanded by multiple acquisitions during the same pass or by dynamic

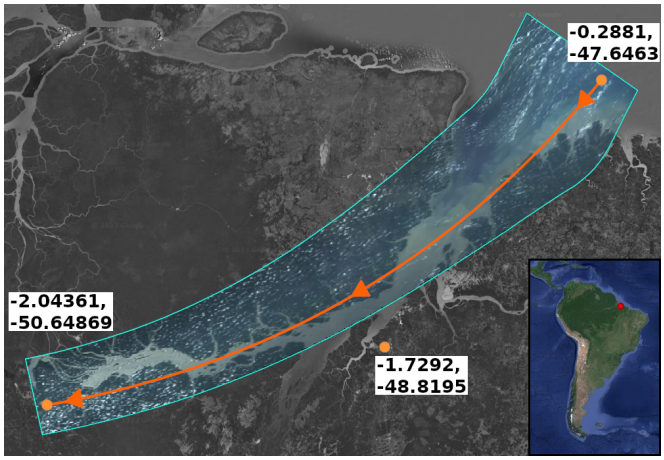

Fig. 22: Manually georeferenced raw data (uncalibrated) RGB composite from capture mode 6-Dynamic-pointing . Orange Line: quadratic Bézier curve to follow. Orange dots: The three control points defining the quadratic Bézier curve. Geodetic latitude, longitude coordinates of the control points indicated. Cyan line: Outline of the recorded data. The satellite ground track is out of frame to the west. (Background imagery ©Google Maps, ©TerraMetrics)

pointing. It has been demonstrated that the capabilities of a commercial-off-the-shelf small satellite can be extended beyond the pre-launch mission design [38].

In order to take full advantage of modes 1-Slewing and 2-Multi-target, further data processing and analysis methods are required, e.g., applying superresolution methods to exploit overlapping data.

Capture mode 2-Multi-target could be extended to consist of more than two image scans during the same pass over the same area. If the same location is sampled many times from multiple angles, the local atmospheric conditions can be sampled more exhaustively, which can inform atmospheric compensation methods.

REFERENCES

[1] B. Seitz, C. Mavrocordatos, et al., "The sentinel-3 mission overview," in *2010 IEEE International Geoscience and Remote Sensing Symposium*, July 2010, pp. 4208–4211.

[2] M. A. Wulder, T. R. Loveland, et al., "Current status of landsat program, science, and applications," *Remote Sensing of Environment*, vol. 225, pp. 127–147, 2019.

[3] R. Loizzo, M. Daraio, et al., "Prisma mission status and perspective," in *IGARSS 2019 - 2019 IEEE International Geoscience and Remote Sensing Symposium*, July 2019, pp. 4503–4506.

[4] T. Fruth, C. Lenzen, E. Gross, and F. Mrowka, *The EnMAP Mission Planning System*, pp. 455–473, Springer International Publishing, Cham, 2019.

[5] M. Lemaître, G. Verfaillie, et al., "Selecting and scheduling observations of agile satellites," *Aerospace Science and Technology*, vol. 6, no. 5, pp. 367–381, 2002.

[6] Z. Lu, X. Shen, et al., "A mission planning modeling method of multipoint target imaging within a single pass for super-agile earth observation satellite," *IEEE Systems Journal*, vol. 16, no. 2, pp. 1921–1932, June 2022.

[7] M. Barnsley, J. Settle, et al., "The proba/chris mission: a low-cost smallsat for hyperspectral multiangle observations of the earth surface and atmosphere," *IEEE Transactions on Geoscience and Remote Sensing*, vol. 42, no. 7, pp. 1512–1520, July 2004.

[8] W. H. Davies, P. R. J. North, W. M. F. Grey, and M. J. Barnsley, "Improvements in aerosol optical depth estimation using multiangle chris/proba images," *IEEE Transactions on Geoscience and Remote Sensing*, vol. 48, no. 1, pp. 18–24, Jan. 2010.

[9] B. G. Henderson and K. S. Krause, "Relative radiometric correction of QuickBird imagery using the side-slither technique on orbit," in *Earth Observing Systems IX*, W. L. Barnes and J. J. Butler, Eds. International Society for Optics and Photonics, 2004, vol. 5542, pp. 426 – 436, SPIE.

[10] D. Liang, J. Yu, B. Han, and H. Zhu, "Side-slither radiometric calibration mode design and in-orbit verification of Ziyuan-1(02D) satellite hyperspectral imager," in *International Conference on Image, Signal Processing, and Pattern Recognition (ISPP 2022)*, M. O. Agyeman and S. Sirkemaa, Eds. International Society for Optics and Photonics, 2022, vol. 12247, p. 122470F, SPIE.

[11] B. A. Kristiansen, D. D. Langer, et al., "Accuracy of a slew maneuver for the hypso-1 hyperspectral imaging satellite - in-orbit results," in *2023 13th Workshop on Hyperspectral Imaging and Signal Processing: Evolution in Remote Sensing (WHISPERS)*, Nov. 2023, pp. 1–5.

[12] T. Xu, X. Yang, et al., "Study of satellite imaging with pitch motion compensation to increase snr," *Optik*, vol. 192, pp. 162933, 2019.

[13] L. Jiang and X. Yang, "Study on enlarging the searching scope of staring area and tracking imaging of dynamic targets by optical satellites," *IEEE Sensors Journal*, vol. 21, no. 4, pp. 5349–5358, Feb. 2021.

[14] R. T. Nallapu, B. Jagatia, et al., "On-orbit demonstrations of proactive tasking of glint imagery," in *2023 IEEE Aerospace Conference*, Mar. 2023, pp. 1–11.

[15] J. Du, X. Yang, et al., "Design of matching imaging on agile satellite with wide-swath whiskbroom payloads along the coastal zone," *Photonics*, vol. 9, no. 12, 2022.

[16] A. Cunningham and R. Legge, "Overview of the agile microsat," in *2021 IEEE Aerospace Conference (50100)*, March 2021, pp. 1–6.

[17] A. Cunningham, R. Legge, and R. Keenan, "Mit lincoln laboratory agile microsat early operations," in *2023 IEEE Aerospace Conference*, March 2023, pp. 1–9.

[18] N. T. Anderson and G. B. Marchisio, "WorldView-2 and the evolution of the DigitalGlobe remote sensing satellite constellation: introductory paper for the special session on WorldView-2," in *Algorithms and Technologies for Multispectral, Hyperspectral, and Ultraspectral Imagery XVIII*, S. S. Shen and P. E. Lewis, Eds. International Society for Optics and Photonics, 2012, vol. 8390, p. 83900L, SPIE.

[19] Maxar, "GeoEye-1 datasheet," 2020, https://resources.maxar.com/data-sheets/geoeye-1, last access: 19 May 2024.

[20] Maxar, "Worldview-3 datasheet," 2020, https://resources.maxar.com/data-sheets/worldview-3, last access: 19 May 2024.

[21] K. Murthy, M. Shearn, et al., "SkySat-1: very high-resolution imagery from a small satellite," in *Sensors, Systems, and Next-Generation Satellites XVIII*, R. Meynart, S. P. Neeck, and H. Shimoda, Eds. International Society for Optics and Photonics, 2014, vol. 9241, p. 92411E, SPIE.

[22] Planet Labs PBC, "Next Generation Satellite Constellation Pelican," 2022, last access: 20 May 2024.

[23] A. Gleyzes, L. Perret, and E. Cazala-Houcade, "Pleiades system is fully operational in orbit," in *2013 European Association of Remote Sensing Laboratories (EARSEL)*, June 2013, pp. 445–460.

[24] Airbus Defence and Space Intelligence, "Pléiades Imagery - User Guide," 2012, USRPHR-DT-125-SPOT-2.0.

[25] Beijing Space View Technology Co.,Ltd. and Siwei Worldview Technology Co.,Ltd., "SpaceView Brochure," https://www.spacewillinfo.com/brochure/SpaceView%20Brochure.pdf, last access: 21 May 2024.

[26] D. Zhang and L. Guo, "A memetic algorithm for single-orbit image scheduling of agile satellite," in *Proceedings of the 2015 5th International Conference on Computer Sciences and Automation Engineering*. 2016/02, pp. 325–329, Atlantis Press.

[27] L. Li, F. Yao, N. Jing, and M. Emmerich, "Preference incorporation to solve multi-objective mission planning of agile earth observation satellites," in *2017 IEEE Congress on Evolutionary Computation (CEC)*, June 2017, pp. 1366–1373.

[28] W. Jun, L. Xiaolu, and H. Lei, "Real-time online rescheduling for multiple agile satellites with emergent tasks," *Journal of Systems Engineering and Electronics*, vol. 32, no. 6, pp. 1407–1420, Dec 2021.

[29] Z. Lu, X. Shen, et al., "Multiple super-agile satellite collaborative mission planning for area target imaging," *International Journal of Applied Earth Observation and Geoinformation*, vol. 117, pp. 103211, 2023.

[30] X. Wang, G. Wu, L. Xing, and W. Pedrycz, "Agile earth observation satellite scheduling over 20 years: Formulations, methods, and future directions," *IEEE Systems Journal*, vol. 15, no. 3, pp. 3881–3892, Sep. 2021.

[31] Z. Lu, X. Shen, D. Li, and Y. Chen, "Integrated imaging mission planning modeling method for multi-type targets for super-agile earth observation satellite," *IEEE Journal of Selected Topics in Applied Earth Observations and Remote Sensing*, vol. 15, pp. 4156–4169, 2022.

[32] R. Vitulli, M. Celesti, et al., "Chime: The first ai-powered esa operational mission," in *Proceedings 4S Symposium*, 2022.

[33] J. Nalepa, M. Myller, et al., "Towards on-board hyperspectral satellite image segmentation: Understanding robustness of deep learning through simulating acquisition conditions," *Remote Sensing*, vol. 13, no. 8, 2021.

[34] G. Giuffrida, L. Fanucci, et al., "The Φ-sat-1 mission: The first on-board deep neural network demonstrator for satellite earth observation," *IEEE Transactions on Geoscience and Remote Sensing*, vol. 60, pp. 1–14, 2022.

[35] D. Evans, "Ops-sat: An esa cubesat," in *Proceedings 4S Symposium*, 2012.

[36] G. Labrèche, D. Evans, et al., "Ops-sat spacecraft autonomy with tensorflow lite, unsupervised learning, and online machine learning," in *2022 IEEE Aerospace Conference (AERO)*, March 2022, pp. 1–17.

[37] J. G. Røysland, D. D. Langer, et al., "Hyperspectral classification onboard the hypso-1 cubesat," in *2023 13th Workshop on Hyperspectral Imaging and Signal Processing: Evolution in Remote Sensing (WHISPERS)*, Nov. 2023, pp. 1–5.

[38] M. E. Grøtte, R. Birkeland, et al., "Ocean color hyperspectral remote sensing with high resolution and low latency–the hypso-1 cubesat mission," *IEEE Transactions on Geoscience and Remote Sensing*, pp. 1–19, 2021.

[39] S. Bakken, M. B. Henriksen, et al., "Hypso-1 cubesat: First images and in-orbit characterization," *Remote Sensing*, vol. 15, no. 3, 2023.

[40] M. Wang, Q. Wu, et al., "Luojia 3-01 satellite—real-time intelligent service system for remote sensing science experiment satellite," *IEEE Journal of Selected Topics in Applied Earth Observations and Remote Sensing*, vol. 17, pp. 8250–8257, Apr. 2024.

[41] R. Gupta and R. Hartley, "Linear pushbroom cameras," *IEEE Transactions on Pattern Analysis and Machine Intelligence*, vol. 19, no. 9, pp. 963–975, Sep. 1997.

[42] E. Ringaby, O. Friman, et al., "Anisotropic scattered data interpolation for pushbroom image rectification," *IEEE Transactions on Image Processing*, vol. 23, no. 5, pp. 2302–2314, May 2014.

[43] O. Egeland and J. T. Gravdahl, *Modelling and Simulation for Automatic Control*, Marine Cybernetics, 2 edition, 2003.

[44] B. Rhodes, "Skyfield," Bibcode: 2019ascl.soft07024R, doi: http://rhodesmill.org/skyfield/, https://pypi.org/project/skyfield/.

[45] D. Q. Huynh, "Metrics for 3D Rotations: Comparison and Analysis," *J Math Imaging Vis*, vol. 35, no. 2, pp. 155–164, Oct. 2009.

[46] A. Dallolio, G. Quintana-Diaz, et al., "A satellite-usv system for persistent observation of mesoscale oceanographic phenomena," *Remote Sensing*, vol. 13, no. 16, 2021.

[47] A. Oudijk, O. Hasler, et al., "Campaign for hyperspectral data validation in north atlantic coastal waters," in *2022 12th Workshop on Hyperspectral Imaging and Signal Processing: Evolution in Remote Sensing (WHISPERS)*, Sep. 2022, pp. 1–5.

[48] D. D. Langer, T. A. Johansen, and A. J. Sørensen, "Consistent along track sharpness in a push-broom imaging system," in *IGARSS 2023 - 2023 IEEE International Geoscience and Remote Sensing Symposium*, July 2023, pp. 4486–4489.

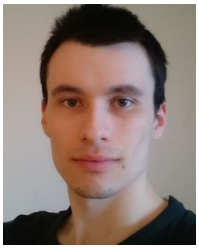

Dennis D. Langer (Member, IEEE) received the B.Sc. degree in electrical engineering from UiT—The Arctic University of Norway, Tromsø, Norway, in 2016, and the M.Sc. degree in industrial cybernetics from the Norwegian University of Science and Technology (NTNU), Trondheim, Norway, in 2019. In 2024, he received the PhD degree from the Department of Marine Technology at NTNU.

His research interests include geometric processing of push-broom satellite data, onboard software for satellite systems, and uncrewed aerial vehicle (UAV) missions with hyperscpectral imager payloads.

Joseph L. Garrett (Member, IEEE) received the B.Sc. degree in physics and mathematics from The Ohio State University, Columbus, OH, USA, in 2011, and the Ph.D. degree in physics from the University of Maryland, College Park, MD, USA, in 2017.

He studies hyperspectral imaging and image processing from satellites and drones as a Researcher with the Norwegian University of Science and Technology (NTNU), Trondheim, Norway.

Bjørn A. Kristiansen (Member, IEEE) received his M.Sc. and Ph.D. degrees from the Norwegian University of Science and Technology in 2019 and 2023, respectively. He is currently a postdoctoral researcher at the NTNU SmallSat lab and the Department of Engineering Cybernetics in Trondheim, Norway. His current research concerns optimization of satellite operations, in particular related to optimal attitude maneuvers and agile satellite operations.

Simen Berg (Graduate student member, IEEE) received his M.Sc. degree in Electronics Systems Design and Innovation at NTNU in 2022. He is currently a PhD Candidate at NTNU where he is researching satellite operations optimization. He is also a Co-Founder of Tycho Space Technologies AS where he works on onboard processing solutions for SmallSats.

Sivert Bakken (Member, IEEE) received the Ph.D. degree with the Department of Engineering Cybernetics, Norwegian University of Science and Technology (NTNU), Trondheim, Norway.

He is researching on how to utilize small satellites with hyperspectral imagers as intelligent agents in coordinated missions involving autonomous agents, and developing methods to advance the usefulness of ocean color data. He is responsible for the software development on HYPSO satellites.

Roger Birkeland (Member, IEEE) received the M.Sc. degree in electronic engineering and the Ph.D. degree in satellite communications from the Norwegian University of Science and Technology (NTNU), Trondheim, Norway, in 2007 and 2019, respectively.

He is a Researcher with the Department of Electronic Systems, NTNU. His main interests are small satellite technologies and systems for optical and RF remote sensing as well as systems for heterogeneous communication for remote areas.

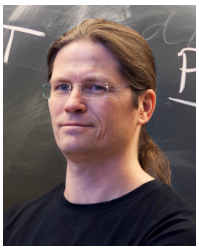

J. Tommy Gravdahl (Senior Member, IEEE) received the Siv.Ing. and Dr.Ing. degrees in engineering cybernetics from the Norwegian University of Science and Technology (NTNU), Trondheim, Norway, in 1994 and 1998, respectively.

He was appointed Associate Professor and Professor with the Department of Engineering Cybernetics, NTNU, in 2001 and 2005, respectively. He was the Head of the Department of Engineering Cybernetics from 2008 to 2009. He has supervised the graduation of 160 M.Sc. and 20 Ph.D. candidates. He has published five books and more than 300 articles in international conferences and journals. His research interests include mathematical modeling and nonlinear control in general, in particular applied to turbomachinery, marine vehicles, spacecraft, robots, and high-precision mechatronic systems.

Dr. Gravdahl received the IEEE Transactions on Control Systems Technology Outstanding Paper Award in 2000 and 2017. He was Senior Editor of the IFAC journal Mechatronics in the period 2017-22 and is since 2020 Associate Editor of the IEEE Transactions on Control Systems Technology.

Tor A. Johansen (Senior Member, IEEE) received the M.Sc. and Ph.D. degrees in electrical and computer engineering from the Norwegian University of Science and Technology (NTNU), Trondheim, Norway, in 1989 and 1994, respectively.

From 1995 to 1997, he worked at SINTEF as a Researcher before he was appointed Associated Professor with the NTNU, in 1997, and a Professor in 2001. He has published several hundred articles in the areas of control, estimation and optimization with applications in the marine, aerospace, automotive, biomedical and process industries. In 2002, he cofounded the company Marine Cybernetics AS, Trondheim, where he was a Vice President until 2008.

Dr. Johansen received the 2006 Arch T. Colwell Merit Award of the SAE and is a Principal Researcher within the Center of Excellence on Autonomous Marine Operations and Systems (NTNU-AMOS), Trondheim, and the Director of the Unmanned Aerial Vehicle Laboratory at NTNU and the SmallSat Laboratory at NTNU. He recently cofounded the spin-off companies Scout Drone Inspection, UBIQ Aerospace, Zeabuz and SentiSystems.

Asgeir J. Sørensen (Senior Member, IEEE) received the M.Sc. degree in marine technology and the Ph.D. degree in engineering cybernetics from the Norwegian University of Science and Technology (NTNU), Trondheim, Norway, in 1988 and 1993, respectively.

He has previously been employed at MARINTEK (currently SINTEF Ocean), Trondheim, Norway, ABB Group (Oslo, Norway/Zürich Switzerland), and Marine Cybernetics (currently DNV), Trondheim, Høvik, Norway. Since 1999, he has been a Professor of marine control systems at the Department of Marine Technology, NTNU. He has authored more than 250 scientific articles and book chapters on marine control systems.